

The GAPS Programme with HARPS-N at TNG. ★

XIII. The orbital obliquity of three close-in massive planets hosted by dwarf K-type stars: WASP-43, HAT-P-20 and Qatar-2. ★★

M. Esposito¹, E. Covino¹, S. Desidera², L. Mancini^{16,3,6}, V. Nascimbeni^{10,2}, R. Zanmar Sanchez⁴, K. Biazzo⁴, A. F. Lanza⁴, G. Leto⁴, J. Southworth⁵, A. S. Bonomo⁶, A. Suárez Mascareño^{7,8}, C. Boccato², R. Cosentino¹¹, R. U. Claudi², R. Gratton², A. Maggio⁹, G. Micela⁹, E. Molinari^{11,14}, I. Pagano⁴, G. Piotto^{10,2}, E. Poretti¹², R. Smareglia¹³, A. Sozzetti⁶, L. Affer⁹, D.R. Anderson⁵, G. Andreuzzi^{11,15}, S. Benatti², A. Bignamini¹³, F. Borsa¹², L. Borsato^{10,2}, S. Ciceri³, M. Damasso⁶, L. di Fabrizio¹¹, P. Giacobbe⁶, V. Granata^{10,2}, A. Harutyunyan¹¹, T. Henning³, L. Malavolta^{10,2}, J. Maldonado⁹, A. Martinez Fiorenzano¹¹, S. Masiero², P. Molaro¹³, M. Molinaro¹³, M. Pedani¹¹, M. Rainer¹², G. Scandariato⁴, and O.D. Turner⁵

¹ INAF – Osservatorio Astronomico di Capodimonte, via Moiariello, 16, 80131 Naples, Italy

² INAF – Osservatorio Astronomico di Padova, Vicolo dell'Osservatorio 5, 35122 Padova, Italy

³ Max-Planck-Institut für Astronomie, Königstuhl 17, D-69117 Heidelberg, Germany

⁴ INAF – Osservatorio Astrofisico di Catania, via S. Sofia 78, 95123 Catania, Italy

⁵ Astrophysics Group, Keele University, Staffordshire, ST5 5BG, UK

⁶ INAF – Osservatorio Astrofisico di Torino, Via Osservatorio 20, I-10025, Pino Torinese, Italy

⁷ Instituto de Astrofísica de Canarias, C/ Vía Láctea, s/n, E38205 - La Laguna (Tenerife), Spain

⁸ Departamento de Astrofísica, Universidad de La Laguna, Avda. Astrofísico Francisco Sánchez, s/n, 38206 La Laguna (TF), Spain

⁹ INAF – Osservatorio Astronomico di Palermo, Piazza del Parlamento, 1, 90134 Palermo, Italy

¹⁰ Dipartimento di Fisica e Astronomia Galileo Galilei – Università di Padova, Vicolo dell'Osservatorio 2, 35122 Padova, Italy

¹¹ INAF – Fundación Galileo Galilei, Rambla José Ana Fernández Pérez 7, 38712 Breña Baja, Spain

¹² INAF – Osservatorio Astronomico di Brera, via E. Bianchi 46, 23807 Merate (LC), Italy

¹³ INAF – Osservatorio Astronomico di Trieste, via G. B. Tiepolo 11, 34143 Trieste, Italy

¹⁴ INAF - IASF Milano, via Bassini 15, 20133, Milano, Italy

¹⁵ INAF - Osservatorio Astronomico di Roma, via Frascati 33, 00040 Monte Porzio Catone (Roma), Italy

¹⁶ Dipartimento di Fisica, Università di Roma Tor Vergata, Via della Ricerca Scientifica 1, 00133 Roma, Italy

Received date / Accepted date

ABSTRACT

Context. The orbital obliquity of planets with respect to the rotational axis of their host stars is a relevant parameter for the characterization of the global architecture of planetary systems and a key observational constraint to discriminate between different scenarios proposed to explain the existence of close-in giant planets.

Aims. In the framework of the GAPS project, we are conducting an observational programme aimed at the determination of the orbital obliquity of known transiting exoplanets. The targets are selected to probe the obliquity against a wide range of stellar and planetary physical parameters.

Methods. We exploit high-precision radial velocity (RV) measurements, delivered by the HARPS-N spectrograph at the 3.6m Telescopio Nazionale Galileo, to measure the Rossiter-McLaughlin (RM) effect in RV time-series bracketing planet transits, and to refine the orbital parameters determinations with out-of-transit RV data. We also analyse new transit light curves obtained with several 1-2m class telescopes to better constrain the physical fundamental parameters of the planets and parent stars.

Results. We report here on new transit spectroscopic observations for three very massive close-in giant planets: WASP-43 b, HAT-P-20 b and Qatar-2 b ($M_p = 2.00, 7.22, 2.62 M_J$; $a = 0.015, 0.036, 0.022$ AU, respectively) orbiting dwarf K-type stars with effective temperature well below 5000 K ($T_{\text{eff}} = 4500 \pm 100, 4595 \pm 45, 4640 \pm 65$ K respectively). These are the coolest stars (except for WASP-80) for which the RM effect has been observed so far. We find $\lambda = 3.5 \pm 6.8$ deg for WASP-43 b and $\lambda = -8.0 \pm 6.9$ deg for HAT-P-20 b, while for Qatar-2, our faintest target, the RM effect is only marginally detected, though our best-fit value $\lambda = 15 \pm 20$ deg is in agreement with a previous determination. In combination with stellar rotational periods derived photometrically, we estimate the true spin-orbit angle, finding that WASP-43 b is aligned while the orbit of HAT-P-20 b presents a small but significant obliquity ($\Psi = 36^{+10}_{-12}$ deg). By analyzing the CaII H&K chromospheric emission lines for HAT-P-20 and WASP-43, we find evidence for an enhanced level of stellar activity which is possibly induced by star-planet interactions.

Key words. Planetary systems – Techniques: spectroscopic, radial velocities – Stars: individual: Qatar-2, WASP-43 and HAT-P-20

★ Based on observations collected at the Italian *Telescopio Nazionale Galileo* (TNG), operated on the island of La Palma by the Fundación

Galileo Galilei of the Istituto Nazionale di Astrofisica (INAF) at the Spanish Observatorio del Roque de los Muchachos of the Instituto de

1. Introduction

The observational study of extrasolar planets flourished in the last two decades and has led to many surprising discoveries that challenged the traditional paradigms of planetary systems formation and evolution. Among those discoveries are the facts that, at variance with what is seen in our Solar System, giant planets can exist very close to their parent stars ($a < 0.1$ AU) and their orbital planes can have large obliquity angles with respect to the host star equatorial planes.

Information on the obliquity of exoplanets is more easily accessed when they happen to transit the host star. Several techniques have been exploited to estimate the orbital obliquity of transiting planets (TPs): star spot crossing (Sanchis-Ojeda & Winn 2011; Mancini et al. 2014), asteroseismology (Chaplin et al. 2013), and gravitational darkening (Barnes et al. 2011). However the great majority of the ~ 100 TPs obliquity measurements¹ were obtained by observing the Rossiter-McLaughlin (RM) effect (Rossiter 1924; McLaughlin 1924). The RM effect is an anomaly in the RV orbital trend occurring during transit, when the planet, by blocking part of the stellar light, causes a distortion of the spectral lines. The shape of the RM anomaly is related to the sky-projected angle λ between the planet orbital axis and the star spin. For a more detailed description of the RM effect see, e.g., Queloz et al. (2000); Ohta et al. (2005); Giménez (2006); Hirano et al. (2010); Boué et al. (2013); Baluev & Shaidulin (2015).

Based on about 50 RM measurements, Albrecht et al. (2012) (see also Winn et al. (2010a) and Schlaufman (2010)) noticed an empirical λ - T_{eff} trend: stars with $T_{\text{eff}} \gtrsim 6250$ K have a broad distribution of obliquities while stars with $T_{\text{eff}} \lesssim 6250$ K are aligned. Most recent RM measurements have substantially confirmed the trend, even though the transition from aligned to oblique orbits appears to be a smoother function of T_{eff} , and some remarkable exceptions have been discovered (Esposito et al. 2014; Winn et al. 2010b).

The NASA Kepler mission has represented a major breakthrough in the field of extrasolar planets science (Borucki 2016). As of now, the number of Kepler candidate transiting planets is larger than 4600 (Coughlin et al. 2016). Even though the majority of them lack the precise RV follow-up needed for the planet mass determination, they constitute a valuable statistical sample and allow to infer important general properties of exoplanetary systems. Kepler found that systems with many transiting planets are common (Lissauer et al. 2011). Simple geometrical considerations lead to believe that the orbits of such planets must be nearly coplanar; Fabrycky et al. (2014), from the analysis of their transit duration ratios, infer that the statistical mode of the orbital mutual inclinations is in the range 1.0–2.2 deg. On the other hand, Morton & Winn (2014), combining the information on stellar rotational period and projected velocity of 70 Kepler objects of interest (KOIs), found with 95% confidence that the obliquities of stars with one transiting planet are systematically larger than those with multiple transiting planets, therewith suggesting that single planets represent dynamically hotter systems than the flat multiple transiting systems. Mazeh et al. (2015) compared the observed amplitude of the rotational photometric

modulation of 993 KOIs with 33,614 single Kepler stars in the temperature range of 3500–6500 K. They found the amplitudes to be statistically higher for KOIs with $3500 \text{ K} < T_{\text{eff}} < 6000 \text{ K}$ and lower for $6000 \text{ K} < T_{\text{eff}} < 6500 \text{ K}$, and interpret this as an indication that cool TP host stars are aligned while hot stars tend to have high obliquities. Their result is in line with what is found by means of RM measurements.

The attempts to explain the observed obliquity distribution of exoplanets have addressed many fundamental open questions of planet formation and evolution, as well as of physics of star interiors. Do giant planets migrate inward by effect of tidal interaction within the protoplanetary disc (Lin et al. 1996; Baruteau et al. 2014) or following planet-planet scattering, Kozai-Lidov cycles, and secular chaotic orbital evolution (Dawson & Murray-Clay 2013; Wu & Lithwick 2011)? Are there mechanisms, such as chaotic star formation (Bate et al. 2010; Thies et al. 2011; Batygin 2012) or stellar internal gravity waves (Rogers et al. 2012), able to misalign the protoplanetary disc plane and the equatorial stellar plane with respect to each other? How effective are star-planet interactions at re-orientating originally misaligned systems (Ogilvie 2014; Lai 2012)? Theoretical efforts will benefit from the characterization of orbital obliquities in correspondence of a wider range of the relevant parameters, such as orbital separation and eccentricity, star and planet mass, stellar effective temperature and metallicity, etc.

We are conducting systematic observations of known transiting planets in the frame of the programme *Global Architecture of Planetary Systems* (GAPS) (Covino et al. 2013; Desidera et al. 2013; Poretti et al. 2016). The selection of our targets is based on the following criteria: i) we give priority to hot-Jupiter systems that allow us to widen the explored range of stellar characteristics (i.e., effective temperature and $\log g$) and planet orbital and physical parameters; ii) in order to guarantee a reliable measurement of the RM effect, we restrict our choice to stars with visual magnitude $V < 14$ mag. We have already presented measurements of the RM effect for six targets in several papers of the GAPS series: Qatar-1b (Covino et al. 2013), HAT-P-18b (Esposito et al. 2014), XO-2b (Damasso et al. 2015a), KELT-6b (Damasso et al. 2015b), HAT-P-36b and WASP-11b (Mancini et al. 2015).

Here we report new observations of the RM effect for three other TPs: WASP-43 b (Hellier et al. 2011), HAT-P-20 b (Bakos et al. 2011) and Qatar-2 b (Bryan et al. 2012). All of them are very massive close-in giant planets (WASP-43 b: $M_p = 2 M_J$, $a = 0.015$ AU; HAT-P-20 b: $7.2 M_J$, 0.036 AU; Qatar-2 b: $2.6 M_J$, 0.022 AU), hosted by dwarf K-type stars with effective temperature well below 5000 K ($T_{\text{eff}} = 4500 \pm 100$, 4595 ± 45 , 4640 ± 65 K respectively). In fact, with the exception of WASP-80 (Triaud et al. 2015), these are the three coolest TP host stars for which the RM effect has been successfully observed. No additional planet is known to orbit around the three host stars, however for HAT-P-20 a long-term RV linear trend was observed (Knutson et al. 2014; Deming et al. 2015), possibly caused by a stellar visual companion. Lucky-Imaging observations (Wöllert & Brandner 2015) put constraints on possible wide companions of WASP-43 and Qatar-2. The high mass of the planets and the small orbital separations also qualify the three systems as interesting candidates to investigate possible stellar activity enhancement induced by the planets.

Astrofísica de Canarias, in the frame of the programme *Global Architecture of Planetary Systems* (GAPS).

** Also based on observations collected at the 0.82m IAC80 Telescope, operated on the island of Tenerife by the Instituto de Astrofísica de Canarias in the Spanish Observatorio del Teide.

¹ We refer to <http://www.astro.keele.ac.uk/jkt/tepcat/rossiter.html> for an updated list of published papers on obliquity measurements.

2. Observations and data reduction

2.1. Spectroscopic data

All the spectra used in this work were acquired with the HARPS-N spectrograph (wavelength coverage: 383–690 nm, resolving power $R=115\,000$), installed at the TNG telescope (Cosentino et al. 2012). The data were reduced by means of the latest version of the HARPS-N Data Reduction Software (DRS) (Cosentino et al. 2014; Smareglia et al. 2014). In addition to 1-D wavelength-calibrated spectra, the DRS provides radial velocities (RVs), calculated by cross-correlating spectra with a numerical mask (Baranne et al. 1996; Pepe et al. 2002; Lovis & Pepe 2007), and line bisectors. The DRS measures also the Mount Wilson S index and, if the stellar B–V colour index is lower than 1.2, also the $\log(R'_{\text{HK}})$ chromospheric activity index is derived (Lovis et al. 2011).

WASP-43. We acquired a time series of 32 spectra, bracketing the transit of WASP-43 b occurring on the 2013 March 11–12 night. With an exposure time of $T_{\text{exp}}=7.5$ minutes, the spectra have a signal-to-noise ratio (S/N) (per pixel in 1-D spectra at 5500 Å) ranging from 12 to 20. Between March 2013 and May 2015 we acquired additional, out-of-transit, spectra at 8 different epochs. The RV measurements were obtained using a K5 mask. A log of the transit observations is reported in Table 1 and all the RVs are shown in Table A.1.

HAT-P-20. A complete transit of HAT-P-20 b was observed on 2014 March 11–12; the time series of 23 spectra, with exposure times of $T_{\text{exp}}=10$ minutes, started ~ 1 hour before ingress and ended ~ 1 hour after egress. The S/N (per pixel in 1-D spectra at 5500 Å) degraded from ~ 25 to ~ 20 during the series, with the increase of the airmass. During the observations the target was close (11 deg) to the almost full (81 %) Moon, and the Moon RV differed from the star RV by only $\sim 8 \text{ km s}^{-1}$, that is ~ 1.1 times the FWHM of the stellar cross-correlation function (CCF). In the CCFs obtained from the sky-illuminated fiber B the Moon peak is visible and the continuum level is about 2% of the stellar CCF continuum. We corrected for the Moon light contamination by subtracting the fiber B CCF from the fiber A CCF, and then measuring the stellar RV by means of a gaussian fit to the CCF difference.

Nineteen additional spectra were taken ($T_{\text{exp}}=15\text{--}20$ minutes, S/N ~ 30) in previous and following nights, spanning a time interval of about 3 years. We estimate that the level of flux contamination in the object fiber from the fainter stellar companion is always well below 10^{-4} . A log of the transit observations is reported in Table 1 and all the RVs are provided in Table A.2.

Qatar-2. A time series of 17 spectra was obtained on 2014 April 27–28 covering a full transit of Qatar-2 b. The exposure time was of 15 minutes, resulting in spectra with S/N ~ 6 (per pixel in 1-D spectra at 5500 Å) and an average RV error of $\sim 30 \text{ m s}^{-1}$. A log of the transit observations is reported in Table 1 and the RVs are shown in Table A.3. We note that the in-transit measurements were taken at lower and nearly constant airmass, while the initial and final out-of-transit data points present a relatively wide air-mass excursion.

2.2. Photometric data

A total of seven new transit light curves are presented in this study, which were acquired with 5 different instruments. A log of the photometric observations is reported in Table 2. Following is a description, case-by-case, of the data acquisition processes and the data reduction techniques.

WASP-43. A complete transit of WASP-43 b was observed on November 25–26 2011 with the Copernico 1.82m telescope, at the Asiago Astrophysical Observatory in northern Italy. The weather conditions were perfect. The 886-frame photometric series, having a constant exposure time of 8 s and a net sampling cadence of about 10 s, was acquired with the AFOSC instrument (Asiago Faint Object Spectrograph and Camera) through a Cousins *R* filter. The PSF was intentionally defocused to about 8 arcsec FWHM. The images were bias/dark subtracted and flat-field corrected using standard techniques. The transit light curve of WASP-43 b was extracted by STARSKY, an independent, customized software pipeline to perform differential aperture photometry over defocused images (Nascimbeni et al. 2011, 2013). The output light curves from STARSKY are automatically normalized by fitting a linear function to the off-transit continuum.

A second complete transit of WASP-43 b was observed on April 15–16 2013 with the CAMELOT imaging camera (*R* filter) mounted on the IAC80 telescope, at the Teide Astronomical Observatory on the Tenerife island (Spain). The exposure time was set to a constant 30 s, resulting in 198 full-frame images and 56 s of net cadence. The PSF was defocused to about 10 pixel FWHM. The images were corrected for bias and flat-field using standard techniques and then processed by STARSKY to get the final, differential light curve.

Another complete transit of WASP-43 b was observed on April 19–20 2013, using the Danish 1.54m telescope at ESO La Silla, Chile, the DFOSC imager, and a Cousins *R* filter. The telescope was operated out of focus (see Southworth et al. (2009) for details of the strategy and its application to this telescope and instrument), and the observations were curtailed immediately after egress in order to capture a time-critical event on another target. The data were reduced using the DEFOT pipeline (Southworth et al. (2014) and references therein), including calibration through master bias and flat-field frames and instrumental flux measurements by aperture photometry. An ensemble comparison star was created from the four good comparison stars in the images, and a linear function of time was applied to rectify the light curve to unit flux outside transit. The weights of the comparison stars, and the coefficients of the linear function, were simultaneously fitted to minimise the scatter in the data outside transit. The resulting light curve has a very low scatter of 0.57 mmag and shows a possible starspot crossing around orbital phase 0.008.

A further complete transit of WASP-43 b was observed with an *R* filter on November 11–12, 2015 within the EXORAP² program carried out at the M. G. Fracastoro Station of the INAF-Catania Astrophysical Observatory with a 80cm f/8 Ritchey-Chretien robotic telescope (APT2), located at Serra la Nave (+14.973°E, +37.692°N, 1725 m a.s.l.) on Mt. Etna, Italy. The telescope is equipped with a set of standard Johnson-Cousins *UBVRI* filters, and an ASPEN camera with a 2k \times 2k e2v CCD 230-42 detector that we operated with a binning factor of 2 (pixel scale 0.94"). Data reduction considered overscan, bias, dark subtraction and flat fielding with the IRAF procedures by using the reduction pipeline specifically developed for the APT2. The

² EXOplanetary systems Robotic APT2 Photometry

Table 1. Log of HARPS-N observations of the planetary transits.

Object	Date ^(a)	UT Start	UT End	N_{obs}	$T_{\text{exp}}[\text{s}]$	Airmass ^(c)	Moon ^(b)	2° fiber
WASP-43	2013-03-11	21:46	02:01	32	450	1.59→1.28→1.46	NO	Sky
HAT-P-20	2014-03-11	21:41	01:41	23	600	1.01→1.85	81%/11°	Sky
Qatar-2	2014-04-27	22:08	02:30	17	900	1.51→1.23→1.41	NO	Sky

Notes. ^(a) Dates refer to the beginning of the night. ^(b) Fraction of illumination and angular distance from the target. ^(c) Values at first→last exposure, or first→meridian→last exposure.

night was not photometric and several frames were removed due to clouds after visual inspection. Fluxes were extracted by aperture photometry as implemented in the IDL routine *aper.pro*. We chose an ensemble of the three least variable stars close to WASP-43 to get its differential photometry. The light curve was normalized to unit flux dividing it by a linear best-fit function of the data outside transit.

HAT-P-20. A nearly complete transit of HAT-P-20 b was observed on January 16-17, 2012 with the CAMELOT camera at the IAC80 telescope through an R filter. The sky was perfectly clear, but a software problem forced the observer to stop the photometric series just 10 min before the last contact of the transit. The camera was set to read-out only one third of the available frame, to minimize the dead time between exposures. The exposure time was set to a constant 15 s, resulting in 483 images and 21 s of net cadence. The PSF was defocused to about 5 pixel FWHM. The images were corrected for bias and flat-field using standard techniques and then processed by STARSKY to get the final, differential light curve.

A complete transit of HAT-P-20 b was observed on October 24-25, 2014 using the Zeiss 1.23 m telescope at Observatory of Calar Alto, Spain, through a Cousins-*I* filter. The telescope was operated out of focus, and the data were reduced using the DEFOT pipeline. Bias and flat-field calibrations were considered but not used as they had a negligible effect on the results except for a slight increase in shot noise. An ensemble comparison star was made from the four good comparison stars in the images, and a quadratic polynomial versus time was applied to rectify the light curve to unit flux outside transit. The weights of the comparison stars, and the coefficients of the polynomial, were simultaneously fitted to minimise the scatter in the data outside transit.

HAT-P-20 presents a complication because of a nearby star, originally noticed in Bakos et al. (2011). Wöllert & Brandner (2015) found it to lie at a separation of 6.925 ± 0.012 arcsec and be fainter than HAT-P-20 in the Gunn *i* and *z* bands by $\Delta i = 2.01 \pm 0.08$ and $\Delta z = 1.67 \pm 0.08$ mag. The point spread function (PSF) of this star partially overlaps that of HAT-P-20. By measuring the PSFs of the two stars, we found that the part of the PSF of the fainter companion within the software aperture for HAT-P-20 produces $18 \pm 6\%$ of the flux of HAT-P-20 in the passband we used for the observations. The light curve was renormalized to correct for the contaminating light from the companion.

Qatar-2. A transit of Qatar-2 b was observed with the IAC80 telescope at the Teide Observatory on April 27-28, 2014, simultaneously to the spectroscopic observations at the TNG. We acquired a series of 133 slightly defocussed frames with the CAMELOT camera in the R-band. Observations were affected by malfunctioning of the automatic dome tracking which caused severe vignetting of the images. We corrected the science frames

for bias and flat field and then extracted relative photometry of our target. We selected the star and sky apertures as well as the set of comparison stars that minimized the scatter in the data outside transit.

For all the light curves, the timestamps were converted into the BJD(TDB) timescale using subroutines provided by Eastman et al. (2010).

3. Stellar parameters

The weighted means of all HARPS-N spectra available for the three targets were used to derive their stellar parameters. In particular, the equivalent widths (EWs) of iron lines taken from the list by Biazzo et al. (2012), together with the *abfind* driver of the MOOG code (Snedden (1973), version 2013), were used to obtain effective temperature (T_{eff}), surface gravity ($\log g$), microturbulence velocity (ξ_{mic}), and iron abundance ($[\text{Fe}/\text{H}]$). This was done by imposing the independence of the iron abundance on the line excitation potentials (for T_{eff}) and EWs (for ξ_{mic}), and the ionization equilibrium between Fe I and Fe II (for $\log g$). The macroturbulence velocity (ξ_{mac}) was fixed to the value obtained using the Valenti & Fischer (2005) relationship depending on T_{eff} and $\log g$. After fixing the stellar parameters at the values derived through the EWs, a spectral synthesis was performed using the *synth* driver of the same code to measure the projected rotational velocity ($V \sin I_{\star}$) and following the prescriptions given by D’Orazi et al. (2011). All the analysis was performed differentially with respect to the Sun, thanks to a mean Vesta spectrum acquired with HARPS-N.

For further details on the procedures based on EWs and spectral synthesis, we refer to the aforementioned papers, together with other works within the GAPS project (see, e.g., Covino et al. (2013); Damasso et al. (2015a); Malavolta et al. (2016)). Results of the spectroscopic analysis here applied to determine the stellar parameters are listed in Table 4.

We used the average spectra also to analyse the CaII H&K lines and measure the chromospheric Mount Wilson S-index for WASP-43 and HAT-P-20, while for Qatar-2 the S/N was too low to derive a reliable measurement. We then calculated the $\log(R'_{\text{HK}})$ index, following the prescriptions in Suárez Mascareño et al. (2015)³. We used our determinations of the T_{eff} and the empirical calibrations reported in Flower (1996) to derive the needed intrinsic B–V colour index. We obtain $B-V = 1.19 \pm 0.06$ and 1.135 ± 0.025 for WASP-43 and HAT-P-20, respectively. We notice that the observed B–V colors (see Table 4) are slightly larger than the intrinsic ones, possibly due to interstellar reddening. The values of the S and $\log(R'_{\text{HK}})$ indices are reported in Table 4.

³ We did not use the HARPS-N DRS for the measurement of the S-index because its application to average spectra is not straightforward. Also, since the B–V colors of our targets are close to 1.2, for the calculation of the $\log(R'_{\text{HK}})$ index, we preferred to follow Suárez Mascareño et al. (2015) rather than Lovis et al. (2011)

Table 2. Log of photometric observations

Object	Instr./Tel.	Filter	Date ^(a)	UT Start	UT End	N_{obs}	$T_{\text{exp}}[\text{s}]$	$T_{\text{cad}}[\text{s}]$ ^(d)	Airmass ^(c)	Moon ^(b)
WASP-43	AFOSC@1.82 m	R	2011-11-25	02:57	05:27	886	8	10	2.28→1.79	NO
"	CAMELOT@IAC80	R	2013-04-15	21:30	00:44	198	30	56	1.29→1.26→1.84	28%/72°
"	DFOSC@Danish 1.5 m	R	2013-04-19	00:02	01:29	49	100	108	1.10→1.06→1.07	67%/26°
"	CCD Camera@APT2 0.8 m	R	2015-11-12	02:09	04:54	73	120	128	2.92→1.52	NO
HAT-P-20	CAMELOT@IAC80	R	2012-01-16	22:29	01:19	483	15	21	1.19→1.00→1.01	NO
"	CCD Camera@CA 1.23 m	I	2014-10-24	02:02	05:33	109	100	111	1.54→1.02	2%/116°
Qatar-2	CAMELOT@IAC80	R	2014-04-27	22:33	02:51	133	90	116	1.43→1.22→1.49	NO

Notes. ^(a) Dates refer to the beginning of the night. ^(b) Fraction of illumination and angular distance from the target. ^(c) Values at first→last exposure, or first→meridian→last exposure. ^(d) Frame acquisition cadence.

4. Light curves and radial velocities analysis

We have developed a code, within the MATLAB software ambient ⁴, for modelling and fitting planet transits observations. The code can simultaneously fit any number of (in- and out-transit) RV data sets, as well as transit light curves in different filters.

The model considers the parameters necessary to fully describe the planet and star position and velocity vectors at any given time, i.e: the masses of the star M_{\star} and of the planet M_p , the orbital period P and eccentricity e , the epoch τ and argument ω of periastron, the systemic RV γ ; the orbital space orientation is described by the inclination angle i_p and the misalignment angle λ . The third angle, the longitude of the ascending node, is not considered as it does not affect the RV and photometric measurements. Other parameters necessary to model the RM effect and the light curves are the radii of the star R_{\star} and of the planet R_p , the stellar projected rotational velocity $V \sin I_{\star}$, and the limb-darkening coefficients. Our model implements each of the 5 equations (linear, quadratic, root-square, logarithmic, and a 4-coefficient law) proposed by Claret & Bloemen (2011) to describe the limb-darkening law. Other effects that can affect the measurements, like stellar surface inhomogeneities (spots, faculae, etc.), stellar differential rotation and convective blue-shift, are not included in the model.

For the analysis of the RM effect we implemented a numerical model based on the following assumptions. We tried to reproduce the observed CCF by modelling an average photospheric line profile. The stellar disc is sampled by a matrix of 1000×1000 elements, each element being represented by a Gaussian line profile with a given width σ_{el} , Doppler-shifted according to the stellar rotation, and weighted by appropriate limb-darkening coefficients. σ_{el} is also a parameter of the fit, however we always fix it, as it turned out that the model RVs are largely insensitive to its exact value. The value of σ_{el} is chosen by adding in quadrature the values of ξ_{mic} and ξ_{mac} . The resulting line profile is then convolved by the instrumental profile of HARPS-N, assumed Gaussian with $\sigma_{IP} = 1.108 \text{ km s}^{-1}$. The model also takes into account the actual area of the stellar photospheric disc occulted and the smearing due to the planet's displacement during an exposure. The corresponding RV shift is then computed by a Gaussian fit of this resulting line profile, analogously to the HARPS-N DRS. The same numerical approach is also used for the modelling and analysis of the light curves. Limb darkening coefficients can be fitted independently for each light curve.

The best-fitting model to the data is found via a sigma-weighted, robust least-squares minimization. The region of the parameters space to be explored can be limited providing upper

and lower limits to the parameter values. Most importantly, any number of linear and non-linear constraints can be set: this allows to place limits to other parameters (such as K , T_{14} , b , etc.), even though they are not direct parameters of the fit. The mass of the star is preliminarily determined from evolutionary track models, adopting the values of the atmospheric parameters determined previously and using the a/R_{\star} value derived from an independent fit of the light curve. The uncertainties on the best-fit values are obtained by means of a bootstrap algorithm.

We use our code to analyse all the RVs and light curves presented in this work. Depending on the type and quality of our data as compared to those in literature, we decide whether a parameter is to be fitted or fixed to the value available in literature.

4.1. WASP-43

To begin with, we analysed the 4 transit light curves (LCs) taken individually. The best-fit values of the relevant parameters are reported in Table 3. Following Sozzetti et al. (2007), we used the a/R_{\star} values to derive the stellar density, resulting in a sigma-clipped weighted average of $\rho_{\star} = 2.47 \pm 0.11 \rho_{\odot}$. The sigma-clipping effectively excluded the APT2 value that is off by $>2\sigma$ with respect to the other three. The stellar density, together with our determinations of T_{eff} and $[\text{Fe}/\text{H}]$, was used to estimate the mass of the star by comparison with the Yonsei-Yale evolutionary tracks (Demarque et al. 2004). Following Southworth (2011), we accounted for systematic uncertainties in the stellar models by adding an extra 5% to the formal errors, and obtained $M_{\star} = 0.688 \pm 0.037 M_{\odot}$.

Our determinations of the 4 epochs of mid-transit are compatible with the most recently published ephemerides (Hoyer et al. 2016; Jiang et al. 2016; Ricci et al. 2015; Chen et al. 2014). In the following analyses, we fixed the orbital period to the value reported in Hoyer et al. (2016), where all the LCs available in literature were analysed homogeneously: $P = 0.813473978 \pm 3.5 \times 10^{-8}$ days.

We then analysed the out-of-transit RVs. In addition to our 22 measurements, we also considered the 23 CORALIE RV values reported in Hellier et al. (2011) and Gillon et al. (2012), allowing for a constant RV offset between the two data sets. We found that the best-fit circular and eccentric orbits were virtually indistinguishable from each other, therefore we opted for fixing $e=0$. Strong constraints on the eccentricity were already put by Gillon et al. (2012) ($0.0035^{+0.0060}_{-0.0025}$) and Blečić et al. (2014) ($0.010^{+0.010}_{-0.007}$), based also on the timing of secondary eclipse. From the best-fit value of the RV curve semi-amplitude $K = 551 \pm 8 \text{ m s}^{-1}$, and the orbital inclination angle that we derived from the LCs analysis (see Table 3), we calculated the planetary mass.

The next step was to analyse the RV time-series covering the planetary transit and to measure the RM effect. By fixing the

⁴ MATLAB R2015b, Optimization Toolbox 7.3 and Curve Fitting Toolbox 3.5.2, The MathWorks, Inc., Natick, Massachusetts, United States.

Table 3. Results of the individual analyses of the four WASP-43 b and two HAT-P-20 b transit light curves. The columns report the following parameters: a/R_\star is the ratio between the semi-major orbital axis and the stellar radius; R_p/R_\star is the planet to star radii ratio; $i[^\circ]$ is the orbital inclination angle; b is the transit impact parameter; T_{14} is the transit duration; T_C is the epoch of mid-transit; u is the coefficient of the linear limb-darkening law according to Equation (1) in Claret & Bloemen (2011).

Instr./Tel.	a/R_\star	R_p/R_\star	$i_p[^\circ]$	T_{14} [days]	T_C [BJD-2400000]	u
WASP-43						
AFOSC@1.82m	4.896 ± 0.084	0.1590 ± 0.0017	82.27 ± 0.29	0.0512 ± 0.0010	55891.67847 ± 0.00018	0.66 ± 0.13
CAMELOT@IAC80	4.989 ± 0.070	0.1594 ± 0.0016	82.12 ± 0.21	0.04943 ± 0.00073	56398.47228 ± 0.00016	0.511 ± 0.075
DFOSC@Danish 1.5m	5.039 ± 0.052	0.15538 ± 0.00086	82.03 ± 0.19	0.04792 ± 0.00036	$56402.539119 \pm 0.000088$	0.484 ± 0.057
CCD Camera@APT2 0.8 m	4.737 ± 0.090	0.1702 ± 0.0021	81.36 ± 0.48	0.05156 ± 0.00030	57339.66239 ± 0.00011	0.54 ± 0.11
HAT-P-20						
CAMELOT@IAC80	10.74 ± 0.44	0.1534 ± 0.0034	86.32 ± 0.40	0.0796 ± 0.0016	55943.52369 ± 0.00025	0.51 ± 0.12
CCD Camera@CA 1.23 m	11.48 ± 0.33	0.1542 ± 0.0027	87.00 ± 0.26	0.0791 ± 0.00048	$56955.634275 \pm 0.000055$	0.675 ± 0.068

other relevant parameters, as obtained by the LCs and out-of-transit RVs fits, we derived a best-fit value for the sky-projected spin-orbit angle λ and stellar rotational velocity $V \sin I_\star$.

Finally, using as a first guess the values obtained from the previous analyses, we made a global joint fit of all the RVs and LCs in order to derive a fully consistent set of best-fit orbital and physical parameters. The final results are reported in Table 4. Aside from our new determination of $\lambda = 3.5 \pm 6.8$ deg, the values of the stellar and planet parameters are consistent with previous measurements (Hellier et al. 2011; Gillon et al. 2012; Chen et al. 2014). The four phase-folded LCs and their best-fit models are displayed in Fig. 1. The RV measurements with the orbital and RM best-fit curves are shown in Fig. 2.

By combining our measurements of R_\star and $V \sin I_\star$ with the stellar rotational period $P_{\text{rot}} = 15.6 \pm 0.4$ days reported in Hellier et al. (2011), we can estimate (see formula (8) in Winn et al. (2007)) the value of $\sin I_\star$ to be 1.08 ± 0.25 . Being $\sin I_\star > 1$ physically impossible, we deduce that the true value of $\sin I_\star$ must be very close to 1. Therefore it is $I_\star \approx 90$ deg, in fact we derive that $I_\star > 72$ deg with a 68% level of confidence. Similarly (see formula (7) in Winn et al. (2007)), we derive that the true orbital misalignment angle Ψ is < 20 deg with a 68% level of confidence.

4.2. HAT-P-20

HAT-P-20 shows clear signatures of a high level of stellar activity. Granata et al. (2014) have analysed the SuperWASP photometry of HAT-P-20 to derive the rotational period and found a modulation with a peak-to-valley amplitude as high as ~ 0.04 mag. Both our two transit light curves show evidence of the planet crossing a star spot (see Fig. 3). Also, the analysis of the RV measurements reveals jitter at the level of $\sim 20 \text{ m s}^{-1}$.

We first analysed the two LCs individually. In Table 3, we report the values of the fitted transit parameters. We find values for R_p/R_\star that are consistent with each other but significantly larger than any of the values reported in Granata et al. (2014). A possible explanation for this discrepancy is that the two transits observed by us occurred during a phase of higher stellar spots filling factor (Ballerini et al. 2012). The two light curves with the best-fit transit model superimposed are displayed in Fig. 3. Thanks to the robust algorithm the best-fit is only marginally affected by the spot crossing regions.

By adding our two determinations of the epoch of mid-transit to the values listed in Granata et al. (2014), we calculated new

transits ephemerides. A weighted least-square linear fit (see Fig. 4) yielded:

$$T_0 (\text{BJD}_{\text{TDB}}) = (2455598.484742 \pm 0.000073) + N(2.87531694 \pm 0.0000019). \quad (1)$$

Fixing the values obtained for T_0 and P , we then performed a global fit of the two light curves and all the HARPS-N RVs. We treated the RV time-series on the night of the transit as an independent data-set by adding a parameter to the fit which represents the barycentric radial velocity for the night of the transit. This was necessary to account for an RV offset most likely caused by the stellar jitters.

The phase-folded RVs and the best-fit model are displayed in the top panel of Fig. 5. Our data confirm that HAT-P-20 b moves on an orbit with a small but significant eccentricity. Our best-fit value is $e = 0.0172 \pm 0.0016$, in agreement with previously reported values ($e = 0.015 \pm 0.005$, Bakos et al. (2011); $e = 0.0158^{+0.0041}_{-0.0036}$, Knutson et al. (2014); $e = 0.0171^{+0.0018}_{-0.0016}$, Deming et al. (2015)). For the mass of the planet we find $M_p = 7.22 \pm 0.36 M_J$, in agreement with the literature value ($M_p = 7.24 \pm 0.18 M_J$, Knutson et al. (2014)). However, given the larger planet radius ($R_p = 1.025 \pm 0.053 R_J$) that we obtain from the transit light curves analysis, we derive a planet density significantly lower ($\rho_p = 8.31 \pm 0.38 \text{ g cm}^{-3}$) than previously reported ($13.78 \pm 1.50 \text{ g cm}^{-3}$, Bakos et al. (2011)). After subtraction of the best-fit 1-planet model, the RV residuals show a scatter ($\text{rms} \approx 16 \text{ m s}^{-1}$) largely exceeding the typical internal RV uncertainties ($\sigma \approx 3.5 \text{ m s}^{-1}$) (see mid-panel in Fig. 5). A frequency analysis of the RV residuals does not point out any significant periodicity, therefore we ascribe the large residuals to stellar activity induced RV jitter. However, we have checked that there is no evident correlation between the RV residuals and the CCF bisector span. In the computation of the errors on the best-fit parameters we accounted for a RV-jitter term. Knutson et al. (2014), with 13 RV measurements spanning 1331 days, report a negative linear trend of $-0.0141^{+0.0073}_{-0.0078} \text{ m s}^{-1} \text{ day}^{-1}$. By allowing for a linear trend in our fit of HARPS-N RVs (19 out-of-transit data points spanning 1137 days), we obtain a positive, but not significant, trend of $7.5\text{e-}03 \pm 15\text{e-}03 \text{ m s}^{-1} \text{ day}^{-1}$.

The best fit model of the RM effect gives $V \sin I_\star = 1.85 \pm 0.27 \text{ km s}^{-1}$, slightly lower but consistent with the spectral synthesis determination, and $\lambda = -8.0 \pm 6.9$ deg which is marginally different from zero. Using the value of the stellar rotational period $P_{\text{rot}} = 14.48 \pm 0.02$ days reported in Granata et al. (2014), we can estimate the stellar spin-axis inclination to be $I_\star = 53 \pm 12$ deg, and the true planet orbital misalignment angle $\Psi = 36^{+10}_{-12}$ deg, meaning that HAT-P-20 b lies on a significantly inclined orbit. As a note of caution on this result, we stress that, if the star experiences a significant differential rotation, we are underestimating

Table 4. Planetary and stellar parameters for the three systems here studied.

Parameter [Unit]	WASP-43	HAT-P-20	Qatar-2
B [mag] ^(j)	13.796 ± 0.022	12.539 ± 0.075	14.582 ± 0.022
V [mag] ^(j)	12.464 ± 0.028	11.339 ± 0.031	13.417 ± 0.023
J [mag] ^(k)	9.995 ± 0.024	9.276 ± 0.022	11.350 ± 0.026
H [mag] ^(k)	9.397 ± 0.025	8.743 ± 0.021	10.794 ± 0.022
K [mag] ^(k)	9.267 ± 0.026	8.601 ± 0.019	10.619 ± 0.021
Space velocity (U, V, W) [km s ⁻¹]	(-2.7, -10.8, -20.4)	(19.1, -27.7, -21.4)	—
<i>Stellar spectra characterization</i>			
Effective temperature, T_{eff} [K]	4500±100	4595±45	4640±65
Surface gravity, $\log g_{\star}$ [cm s ⁻²]	4.50±0.20	4.52±0.09	4.51±0.12
Iron abundance, [Fe/H]	-0.01±0.15	0.22±0.09	0.13±0.10
Microturbulence vel., ξ_{mic} [km s ⁻¹]	1.00±0.15	0.74±0.27	0.90±0.35
Macroturbulence vel., ξ_{mac} [km s ⁻¹] ^(l)	2.03	2.17	2.24
Proj. rot. vel., $V \sin I_{\star}$ [km s ⁻¹]	2.6±0.5	2.0±0.5	2.0±1.0
<MW S-index>	1.647±0.059	1.20±0.13	—
<log(R'_{HK})>	-4.35±0.10	-4.40±0.06	—
<i>RV and photometric data fit</i>			
Star mass, M_{\star} [M _⊙]	0.688 ± 0.037	0.742 ± 0.042	0.798 ± 0.040
Planet mass, M_{p} [M _J]	1.998 ± 0.079	7.22± 0.36	2.616 ± 0.071
Star radius, R_{\star} [R _⊙]	0.6506 ± 0.0054	0.6796 ± 0.0054	0.793 ± 0.024
Planet radius, R_{p} [R _J]	1.006 ± 0.017	1.025 ± 0.053	1.281 ± 0.039
Orbital period, P [days]	0.813473978±0.000000035 ^(a)	2.875316938±0.000000019	1.33711647 ± 0.000000026 ^(f)
Eccentricity, e	0 (fixed)	0.0172 ± 0.0016	0 (fixed)
Longitude of periastron, ω [deg]	90 (fixed)	342.7 ± 7.3	90 (fixed)
Orbital inclination, i_{p} [deg]	82.109 ± 0.088	86.88 ± 0.31	86.12 ± 0.08 ^(f)
Epoch of periastron, τ [BJD]	—	2455942.681 ± 0.016	—
Barycentric RV, γ [m s ⁻¹]	-3595.5 ± 4.3 ^(b)	-18087.44 ± 0.7 ^(g)	-23977.5 ± 7.1
Barycentric RV, γ_2 [m s ⁻¹]	-3588.1 ± 2.7 ^(c)	-18093.36 ± 0.8 ^(g)	—
Proj. spin-orbit angle, λ [deg]	3.5 ± 6.8	-8.0 ± 6.9	15 ± 20
Proj. rot. vel., $V \sin I_{\star}$ [km s ⁻¹]	2.26 ± 0.54	1.85 ± 0.27	2.09 ± 0.58
Stellar rotational period, P_{rot} [days]	15.6±0.4 ^(d)	14.48±0.02 ^(e)	18.77 ± 0.29
<i>Derived parameters</i>			
Orbital semi-major axis, a [AU]	0.01504 ± 0.00029	0.03593 ± 0.00029	0.02205 ± 0.00037
Transit duration, T_{14} [days]	0.0485 ± 0.010	0.07900 ± 0.00052	—
Impact parameter, b	0.689 ± 0.013	0.622 ± 0.059	0.405 ± 0.028
a/R_{\star}	4.97 ± 0.14	11.36 ± 0.25	5.98 ± 0.28
R_{p}/R_{\star}	0.1588 ± 0.0040	0.155± 0.010	0.166 ± 0.010
Spin-orbit angle Ψ [deg]	<20 ⁽ⁱ⁾	36 ⁺¹⁰ ₋₁₂	<43 ⁽ⁱ⁾
Star incl. angle I_{\star} [deg]	>72 ⁽ⁱ⁾	53 ± 12	>58 ⁽ⁱ⁾
RV-curve semi-amplitude, K [m s ⁻¹]	551.0±3.2	1249.5± 1.2	558.7 ± 5.9 ^(h)
Star density, ρ_{\star} [g cm ⁻³]	2.526 ± 0.080	2.36 ± 0.16	2.240 ± 0.023 ^(f)
Star surface gravity, $\log g_{\star}$ [cm s ⁻²]	4.647 ± 0.011	4.643± 0.020	4.541± 0.048
Planet density, ρ_{p} [g cm ⁻³]	2.43 ± 0.14	8.31 ± 0.38	1.54 ± 0.20
Planet surface gravity, $\log g_{\text{p}}$ [cm s ⁻²]	3.696 ± 0.018	4.231 ± 0.019	3.597 ± 0.038
Planet equilibrium temperature, T_{p} [K]	1426.7 ± 8.5	964 ± 10	1342 ± 15

Notes. ^(a) Adopted from Hoyer et al. (2016); ^(b) CORALIE data; ^(c) HARPS-N data; ^(d) Adopted from Hellier et al. (2011); ^(e) Value adopted from Granata et al. (2014), error derived by us with an independent re-analysis of the data; ^(f) Adopted from Mancini et al. (2014); ^(g) Off-transit (γ) and in-transit (γ_2) HARPS-N data; ^(h) Adopted from Bryan et al. (2012); ⁽ⁱ⁾ At the 68% level of confidence. ^(j) APASS catalogue (Henden et al. 2016). ^(k) 2MASS catalogue (Cutri et al. 2003). ^(l) Fixed to the values obtained following Valenti & Fischer (2005)

$V \sin I_{\star}$, while higher values of $V \sin I_{\star}$ translate in I_{\star} closer to 90 deg and Ψ closer to 0 deg.

4.3. Qatar-2

The Qatar-2 b transit photometry, which we acquired simultaneously to the HARPS-N RV monitoring, resulted to be affected by a trend that starts shortly after the mid-transit phase and extends well beyond the end of the transit (see the top panel in Fig. 6). We traced back the origin of this trend to image vignetting (see Section 2.2), but we could not reliably model and correct for it.

Therefore, although we show the light curve, it was not actually used in our data fit. Instead, we adopted the relevant parameters from Mancini et al. (2014), who analysed a series of high quality transit light curves of Qatar-2 b (see Table 4). Specifically, we used the stellar density $\rho_{\star} = 2.240 \pm 0.023$ g cm⁻³ from Mancini et al. (2014), together with our spectroscopic determinations of T_{eff} and [Fe/H], as input to the Yonsei-Yale evolutionary tracks to estimate the stellar mass $M_{\star} = 0.798 \pm 0.040$ M_⊙ and radius $R_{\star} = 0.793 \pm 0.024$ R_⊙. Then, we consistently scaled the values of the planet mass $M_{\text{p}} = 2.616 \pm 0.071$ M_J and radius $R_{\text{p}} = 1.281 \pm 0.039$ R_J. As a check, we verified that the light curve model, cal-

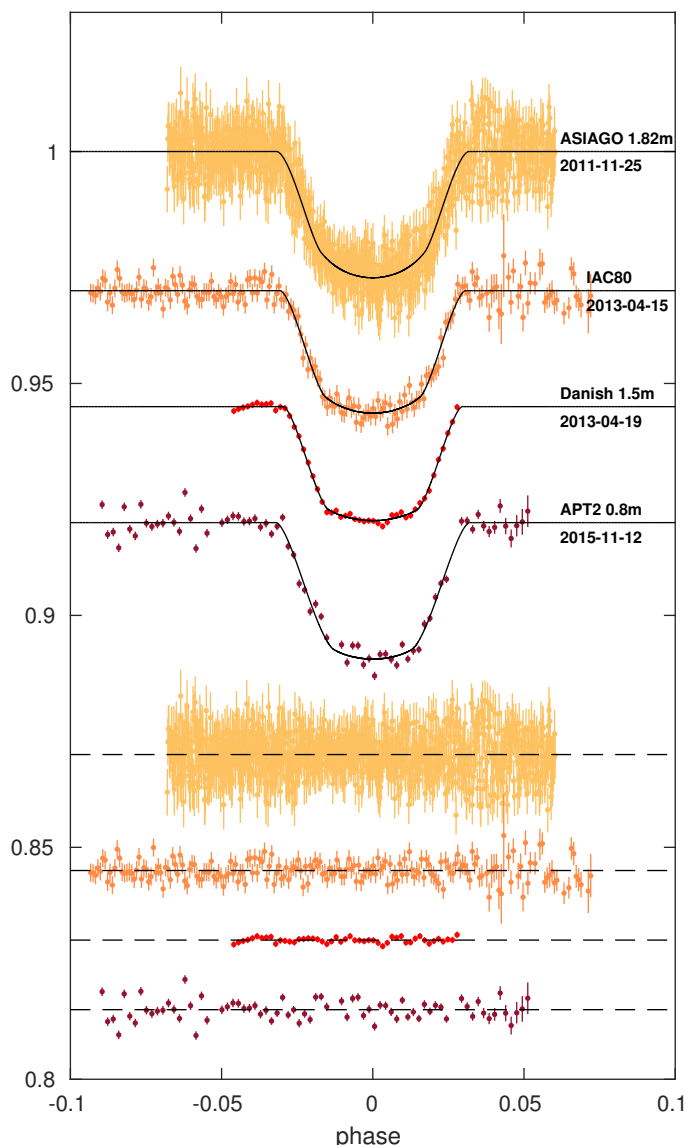


Fig. 1. WASP-43 normalized light curves with best-fit models superimposed. For clarity a vertical offset was applied to the different LCs. The lower part of the diagram shows the best-fit residuals. Data are phase-folded according to the orbital period reported in Table 4 and the epochs of mid-transit reported in Table 3. For each LC we report the telescope and the date of observation. In all cases a Johnson R filter was used.

culated adopting those parameters, adjusts well to the first half of our IAC80 photometric data (see top panel in Fig. 6).

The RV time-series covering the Qatar-2 b transit was fitted with the RM model, setting free only three parameters: λ , $V \sin I_*$ and γ . The best-fit values are reported in Table 4 and the RV measurements with the best-fit solution are displayed in the middle panel of Fig. 6. With only 8 in-transit data points and relatively large RV errors, as compared with the amplitude of the RM effect, our detection may not appear statistically significant. However, we note that the best-fit value of $V \sin I_* = 2.09 \pm 0.58 \text{ km s}^{-1}$ agrees with the value of $2.0 \pm 1.0 \text{ km s}^{-1}$ derived from our spectroscopic analysis. In order to assess the reliability of our estimate of $\lambda = 15 \pm 20 \text{ deg}$, we then computed RM models with $V \sin I_*$ fixed to 2.0 km s^{-1} for three different values of λ (90, 180, -90 deg), shown in Fig. 6. By comparing the different models, it appears that the data allow us to discriminate between different values of λ . Furthermore, we note that the

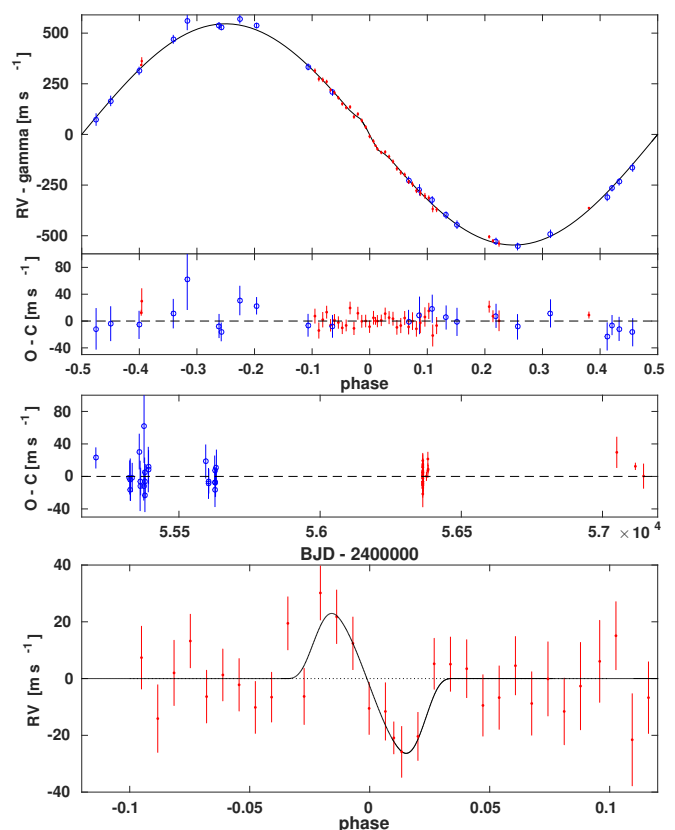


Fig. 2. WASP-43 radial velocities. Red dots represent HARPS-N data while blue open circles are CORALIE data. *Top panels:* phase-folded RVs with the best-fit RV curve superimposed, and below the corresponding residuals. *Middle panel:* RV residuals plotted as a function of the Barycentric Julian Date (BJD) show no evidence of a long term RV trend. *Bottom panel:* Zoom in the RV time-series covering the transit. In order to highlight the RM effect, the orbital RV trend was subtracted.

best-fit value of λ we obtain is consistent with a previous determination of $\lambda = 4.3 \pm 4.5 \text{ deg}$, obtained by Mancini et al. (2014) using the spot crossing method.

4.3.1. Stellar rotational period

We retrieved the publicly available QES (Qatar Exoplanet Survey) photometric monitoring data of Qatar-2 (Bryan et al. 2012). The time-series consists of 1217 data points distributed over 54 nights and spanning an interval of 84 days. After removing some evident outliers (44 points), we analysed the remaining points for possible periodic signals, both before and after removing the in-transit data ($-0.04 < \text{phase} < 0.04$; 94 points). The Lomb-Scargle periodograms (top panel in Fig. 7) show two peaks, which become prominent after discarding the in-transit points, corresponding to periods $P_1 \sim 18.7$ days and $P_2 \sim P_1/2$. In order to assess the significance of these peaks, we computed the periodograms for 10^5 mock data sets, obtained by randomly permuting the time-stamps of the original data set. Then, we calculated false alarm probability (FAP) levels; for instance, a 1% FAP level means that in 10^3 out of 10^5 cases a peak higher than that level was found in the periodograms, over the entire frequency range $[10^{-3}, 1.02] \text{ days}^{-1}$. In this way, we estimate the FAP associated with the peak at P_1 to be 0.9%. In the bottom panel of Fig. 7 we show the Qatar-2 QES photometry, binned on a night-by-night basis, phase-folded with the period P_1 and an arbitrarily chosen reference epoch. We consider P_1 as the stellar

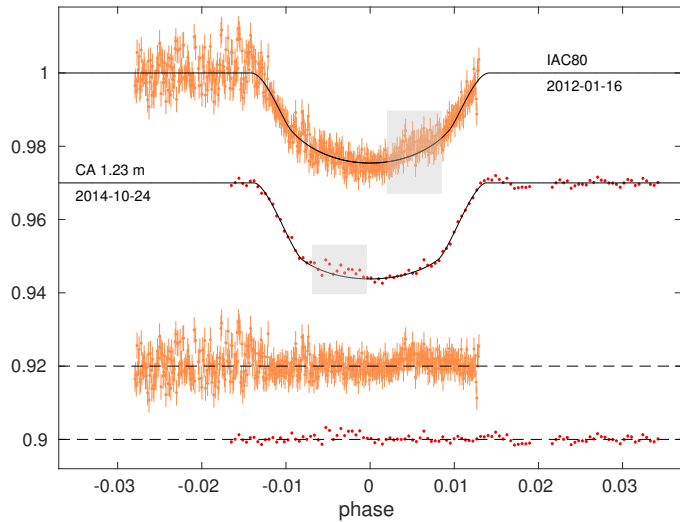


Fig. 3. HAT-P-20 light curves (top) and best-fit residuals (bottom). Data are phase-folded according to the best-fit period reported in Eq. (1). For each LC the telescope and date of observation are indicated. For the IAC80 LC a Johnson-*R* filter was used, for the CA LC a Cousins-*I* filter. Shaded areas indicate phases of possible spot crossing.

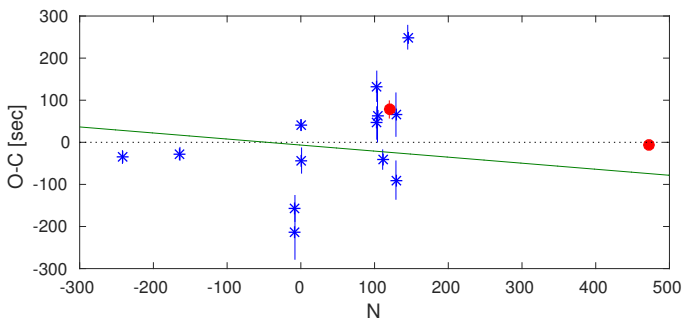


Fig. 4. O-C diagram obtained by a linear fitting (i.e constant period) of the HAT-P-20 b mid-transit epochs. Blue asterisks are from Granata et al. (2014), red dots correspond to the two transit observations reported in this work. The green continuous line represents the ephemerides calculated in Granata et al. (2014).

rotational period. The light curve shows a clear minimum around phase 0.5 and then a rather flat maximum from 0.8 to 0.3. The strong harmonic at $P_1/2$ observed in the periodogram also points to an asymmetric light curve. This shape can be explained by a single cold spotted region visible for half period only, perfectly compatible with the equator-on orientation of our line of sight. We used a bootstrap method, applied to the binned data, to derive the uncertainty on the period, obtaining $P_{\text{rot}} = 18.77 \pm 0.29$ days. Very recently two independent works (Močnik et al. 2016; Dai et al. 2016) reported on the analysis of K2 photometric time-series for Qatar-2, and both determined a stellar rotational period in agreement with our result, and confirmed that the planet is aligned.

Using the values of P_{rot} , $V \sin I_*$, and R_* , we derive that $I_* > 58$ deg with a 68 % confidence level. From our determination of $\lambda = 15 \pm 20$ deg, we estimate that the true spin-orbit angle is $\Psi < 43$ deg with a 68 % confidence level.

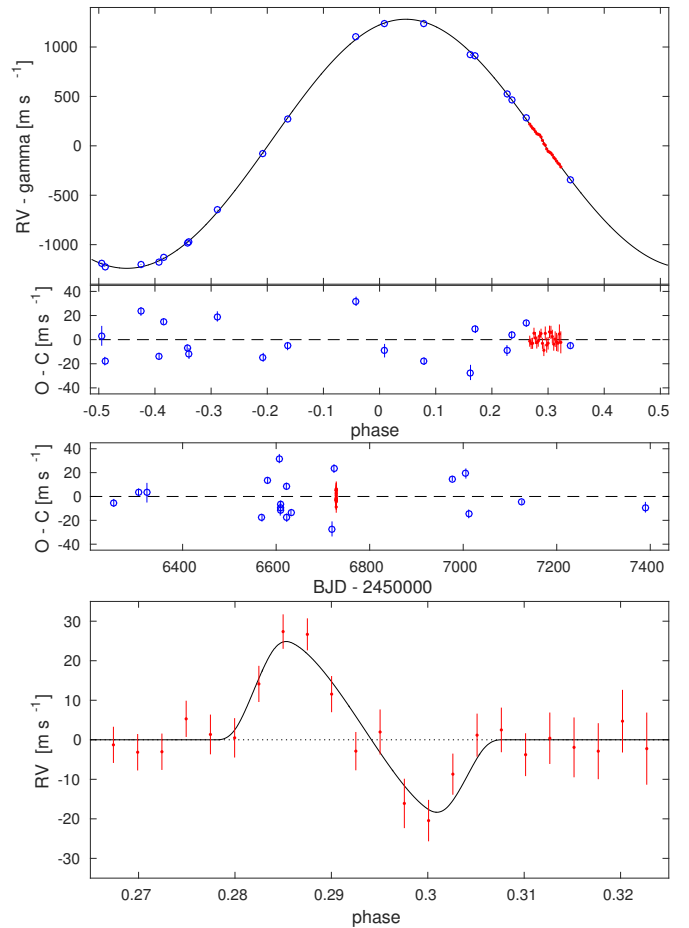


Fig. 5. HAT-P-20 radial velocities. Data taken during the night of the transit are displayed with red dots. *Top panels:* phase-folded RVs with the best-fit RV curve superimposed, and below the corresponding residuals. *Middle panel:* RV residuals plotted as a function of the Barycentric Julian Date (BJD) show no evidence of a long term RV trend. *Bottom panel:* RV time-series covering the transit. In order to highlight the RM effect, the orbital RV trend was subtracted.

5. Discussion

5.1. Stellar activity

It has been speculated that the presence of close in giant planets could cause an enhancement of the activity level of their host stars, via star-planet tidal interactions and/or magnetic coupling (Cuntz et al. 2000; Lanza 2008, 2012). Many observational studies have looked for correlations between stellar activity indicators and the presence and properties of exoplanets (e.g. Maggio et al. (2015); Borsa et al. (2015)). Shkolnik (2013), considering the 272 known FGK planetary hosts observed by GALEX, found only tentative evidence that hot-Jupiters host stars are more FUV-active; Poppenhaeger et al. (2010), analyzing planet-bearing stars within 30 pc, concluded that there are no correlations of X-ray luminosity or the activity indicators L_X/L_{bol} with planetary parameters. Krejčová & Budaj (2012) found statistically significant evidence that the equivalent width of the Ca II K line emission and $\log(R'_{\text{HK}})$ activity parameter of the host star vary with the mass and orbital semi-major axis of the planet. In a similar study, which considered however a sample of planets at larger orbital separations, Canto Martins et al. (2011) had not found significant correlations.

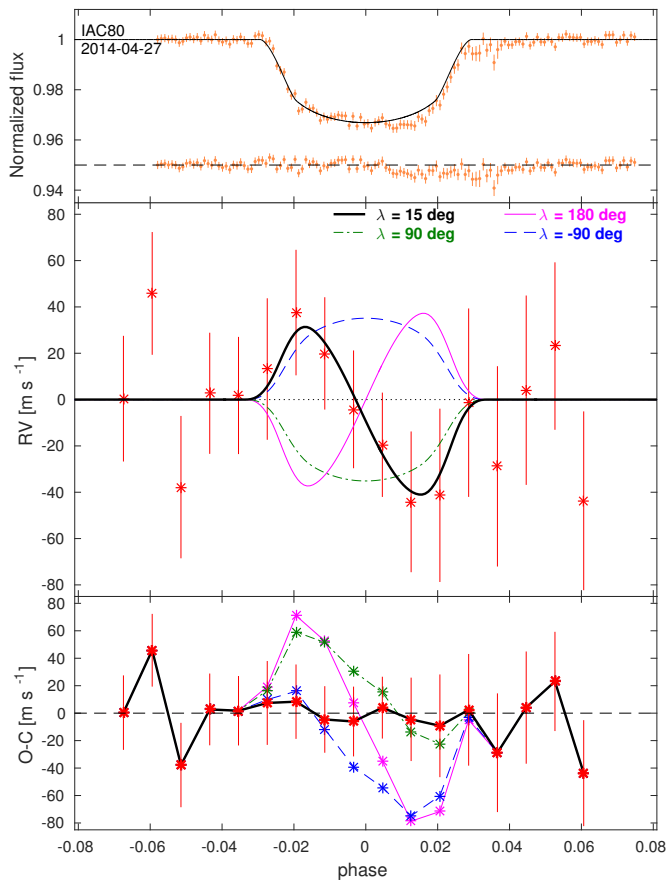


Fig. 6. Simultaneous photometric and RV monitoring of the transit of Qatar-2b. Top panel: IAC80 photometric data. The black line is the model light curve, but it is not a fit to the data (see text in Sec. 4.3 for details). Middle panel: RV time-series covering the transit (red asterisks). In order to highlight the RM effect, the orbital RV trend was subtracted. Together with our best-fit model (black thick line), we show also models with $V \sin I_* = 2.0 \text{ km s}^{-1}$ and $\lambda = -90, 90, 180 \text{ deg}$ (dashed blue, dot-dashed green, magenta lines, respectively). Bottom panel: RV residuals for the best-fit model of the RM effect and for the other three models shown in the middle panel.

We have found that HAT-P-20 and WASP-43 have values of $\log(R'_{\text{HK}})$ (see Table 4) that place them among the most active planet-host stars, reinforcing the Krejčová & Budaj (2012) results (see in particular their Figure 3 and 5). Suárez Mascareño et al. (2015), by studying a sample of stars monitored with the HARPS spectrograph for which the presence of hot-Jupiters can be excluded with high confidence, found an empirical tight correlation between the stellar rotational period P_{rot} and the average $\log(R'_{\text{HK}})$ (see also Noyes et al. (1984) and Mamajek & Hillenbrand (2008)). According to their Equation (9), based on the measured P_{rot} , WASP-43 and HAT-P-20 should have a $\log(R'_{\text{HK}})$ of -4.62 ± 0.07 and -4.57 ± 0.07 respectively, lower than the measured values by 0.27 ± 0.12 and 0.17 ± 0.08 respectively. Thus, we have found that, at the $2\text{-}\sigma$ level of confidence, both WASP-43 and HAT-P-20 show an enhanced level of chromospheric activity as measured by the $\log(R'_{\text{HK}})$ index. The excess of activity could be an effect of the young age of the stars. Due to the late spectral type of the stars, evolutionary models are unable to provide stringent constraints on their age. However, we calculated the Galactic space velocities (see Table 4) using the spectroscopic parallaxes reported in Hellier et al. (2011) and Bakos et al. (2011) for WASP-43 and HAT-P-20, respectively. Both stars have space

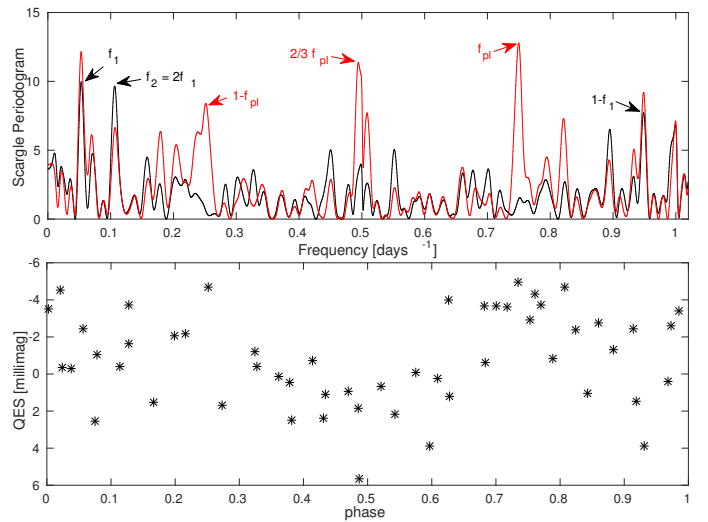


Fig. 7. Top panel: Scargle periodogram of the QES photometric monitoring data of Qatar-2, before (red line) and after (black line) removing the in-transit points. f_{pl} corresponds to the planet orbital period; we deem the peak at f_1 to originate from a photometric modulation at the stellar rotational period. Bottom panel: Nightly averaged photometric data phase-folded at the $P_1 \equiv 1/f_1 = 18.77$ days period.

velocities not compatible with any of the known nearby young moving groups (Zuckerman & Song 2004). We conclude that the origin of the enhanced activity is likely to be sought in the tidal and/or magnetic interactions of the stars with their close-in massive planetary companions.

5.2. Obliquity and stellar rotation

In Fig. 8 we have revisited and updated the diagrams in Fig. 1 of Dawson (2014). Our diagrams also differ in that we did not apply the cuts in planet mass ($M_{\text{pl}} > 0.5 M_J$) and period ($P > 7$ days) used in Dawson (2014). We stress that all the three stars studied in this work have $T_{\text{eff}} \sim 4500 \text{ K}$, hence they populate a region of the λ - T_{eff} diagram that was largely unexplored before. Our three targets show small obliquities, therefore, considering also the relatively high mass and short orbital period of their planets, they appear consistent with the λ - T_{eff} trend, according to which planets around stars with $T_{\text{eff}} \lesssim 6250 \text{ K}$ have aligned orbits (Albrecht et al. 2012).

Dawson (2014) noticed that for $T_{\text{eff}} \lesssim 6000 \text{ K}$, out of 19 systems with known λ , the 2 with the highest values of the projected stellar angular rotational velocity $\Omega_* \sin I_*$ corresponded to the most massive planets (CoRoT-2b and CoRoT-18b)⁵. She argued that this was the result of a planet mass dependence of the stellar projected rotation frequencies for cool stars, with massive planets being able to spin up their host stars via tidal interaction, contrasting the magnetic braking. She was able to reproduce this and other observational trends in a theoretical framework in which, for cool stars, the mass dependence was insensitive to the stellar T_{eff} (see right bottom diagram of her Fig. 1). However, our targets, in particular HAT-P-20 and Qatar-2, in spite of the large mass of the planets, have small values of $\Omega_* \sin I_*$ (see the bottom panel of Fig. 8). This suggests that probably, at the temperatures of our targets ($T_{\text{eff}} \sim 4500 \text{ K}$), the magnetic braking

⁵ The third massive planet shown in Fig. 8 is HD80606b: with an orbital period of ~ 111 days, it is not expected to have any significant tidal interactions with its host star.

dominates over tidal spin up; a larger number of similar systems should be studied to settle this issue.

5.3. Tidal timescales

All our systems are currently not synchronized, i.e., far from tidal equilibrium. In principle, only HAT-P-20 could reach a stable equilibrium because its total angular momentum is very close to the minimum value required according to Hut (1980), while for WASP-43 and Qatar-2 it is smaller by a factor of about two. However, given the steady angular momentum loss produced by the magnetized wind in late-type stars, such a stable equilibrium, even if established, cannot be maintained in HAT-P-20 (Damiani & Lanza 2015). Since the orbital periods of the three systems are shorter than the rotation periods, tides transfer angular momentum from the orbit to the stellar spin and the fate of these close-in planets is to fall towards their host stars.

An estimate of the infall timescale in our systems is made very uncertain by our ignorance of the physics of the dissipation of tidal kinetic energy inside late-type stars and planets, in particular of the dissipation of dynamical tides, i.e., the wave-like perturbations excited by the tidal potential that varies periodically in the reference frame of the stars and planets (Ogilvie 2014). We parameterize the efficiency of tidal dissipation by means of the so-called modified tidal quality factors, Q'_s and Q'_p for the star and the planet, respectively. In close binary systems consisting of two late-type stars, the observations suggest $Q'_s \approx 10^6$ (Ogilvie & Lin 2007) that would imply a short remaining lifetime for all our three systems, ranging from ~ 13 Myr for WASP-43 to ~ 900 Myr for HAT-P-20 (Metzger et al. 2012, from Eq. (1) in). The e-folding timescale for the decrease of any initial obliquity of our systems would be comparable or shorter, ranging from ~ 10 Myr for WASP-43 to 160 Myr for HAT-P-20, if we adopt the constant time-lag model of Leconte et al. (2010) and the presently measured parameters of the systems (cf. Table 4)⁶.

An observational lower limit $Q'_s \gtrsim 10^5$ for WASP-43 has been obtained by Hoyer et al. (2016), but it is far too low to be useful in our context. Assuming a likely tidal spin-up of the host star in the HATS-18 system, Penev et al. (2016) estimate Q'_s for that solar-like host. Scaling their value according to the different rotation periods of our target host stars based on the inertial wave dissipation model by Ogilvie & Lin (2007), we assume $Q'_s = 10^7$, while $Q'_p = 10^6$ is appropriate for WASP-43 b and Qatar-2 b, and $Q'_p = 5 \times 10^6$ for HAT-P-20 b in view of its longer period, by scaling from the value of $Q'_p \approx 10^5$ for Jupiter (Ogilvie 2014, see, Sect. 5.4 in). A $Q'_s \sim 10^7$ is also in general agreement with the statistical study by Jackson et al. (2009). With such values of the modified tidal quality factors, we obtain remaining lifetimes ranging from ~ 130 Myr for WASP-43 to ~ 9 Gyr for HAT-P-20. The expected $O - C$ of the epoch of mid-transit with respect to a constant-period ephemeris is the largest for WASP-43 and it is of -5.5 s in ten years. The e-folding decay time of the initial obliquity ranges from ~ 100 Myr for WASP-43 to ~ 1.6 Gyr for HAT-P-20, i.e., shorter than the probable ages of the systems, thus suggesting that tides could have had enough time to align any initially oblique spin of the stars. On the other hand, the dissipation of any initial orbital eccentricity is dominated by the tides inside the planets and the corresponding e-folding timescales are shorter than ~ 10 Myr for WASP-43 and

Qatar-2, while it is of ~ 4 Gyr in the case of HAT-P-20, suggesting that its present non-zero eccentricity could have been excited when the system formed.

As mentioned in Sec. 2.2, HAT-P-20 has a visual companion at an angular separation of 6.9 arcsec. In the URAT catalog (Nicholson 2015; Zacharias et al. 2015), HAT-P-20 and its companion are reported to have a common proper motion, separation $\rho = 6.93$ arcsec and position angle $PA = 320.6$ deg at the epoch $TE = 2013.865$ yr. Previous observations indicated similar values: $\rho = 6.939$ arcsec, $PA = 320.6$ deg, $TE = 2001.068$ yr (Hartkopf et al. 2013); $\rho = 6.860$ arcsec, $PA = 320.3$ deg, $TE = 1998.07$ yr (Wycoff et al. 2006). Thus, in all probability the two stars are physical companions; at an estimated distance of 70 ± 3 pc (Bakos et al. 2011), the two stars have a projected separation of ~ 490 AU. The stellar companion, based on its 2-MASS colors, is an M-dwarf (Salz et al. 2015). It can not be excluded that gravitational perturbations from the companion played a role in the orbital evolution of HAT-P-20 b leading to the current slightly eccentric and misaligned orbit.

6. Conclusions

We have measured the RM effect for the close-in and massive transiting planets orbiting WASP-43, HAT-P-20 and Qatar-2, three K-dwarf stars with effective temperatures of 4500, 4595 and 4640 K, respectively. We have found that the true spin-orbit angle Ψ of WASP-43 b is consistent with zero. For Qatar-2 b, we only report a marginal detection of the RM effect, however our results support previous evidence that the system is aligned. HAT-P-20 b, the one among the three with the largest semi-major axis, has small but significant eccentricity ($e = 0.0172 \pm 0.0016$) and obliquity ($\Psi = 36^{+10}_{-12}$ deg) which might be related to the presence of the stellar companion at projected separation of ~ 490 AU.

HAT-P-20 and WASP-43, for which we could obtain reliable measurements of the average R'_{HK} index, show an activity level exceeding the values typical for stars with the same rotation period. We take this as a likely manifestation of either tidal or magnetic star-planet interactions. A larger number of spectra with higher S/N would be needed to study the R'_{HK} variability and possible modulations with the planet orbital phase.

Contrarily to what has been observed in two stars with $T_{\text{eff}} \sim 5500$ K hosting massive planets, our targets do not show clear evidence of stellar rotational spin-up.

Overall, our findings are consistent with the scenario in which star-planet interactions have been effective in circularizing and aligning the planetary orbits, similarly to what already observed for hotter stars up to $T_{\text{eff}} \sim 6250$ K.

Acknowledgements. We thank the anonymous referee for her/his useful comments and suggestions. The GAPS project in Italy acknowledges the support by INAF through the "Progetti Premiali" funding scheme of the Italian Ministry of Education, University, and Research. Based on observations collected at Copernico telescope (Asiago, Italy) of the INAF - Osservatorio Astronomico di Padova. V. N. acknowledges partial support by the Università di Padova through the "Studio preparatorio per il Plato Input Catalog" grant (#2877-4/12/15) funded by the ASI-INAF agreement (n. 2015-019-R.0). The authors acknowledge Dr J.M. Alcalá, Dr. L. Bedin and Dr. G. Lodato for their comments and suggestions.

References

- Albrecht, S., Winn, J. N., Johnson, J. A., et al. 2012, *ApJ*, 757, 18
- Bakos, G. Á., Hartman, J., Torres, G., et al. 2011, *ApJ*, 742, 116
- Ballerini, P., Micela, G., Lanza, A. F., & Pagano, I. 2012, *A&A*, 539, A140
- Blauvelt, R. V. & Shaidulin, V. S. 2015, *MNRAS*, 454, 4379

⁶ We computed the constant time lag τ using Eqs. (18) and (19) in Leconte et al. (2010) and assuming that the planet rotation is synchronous with the orbit.

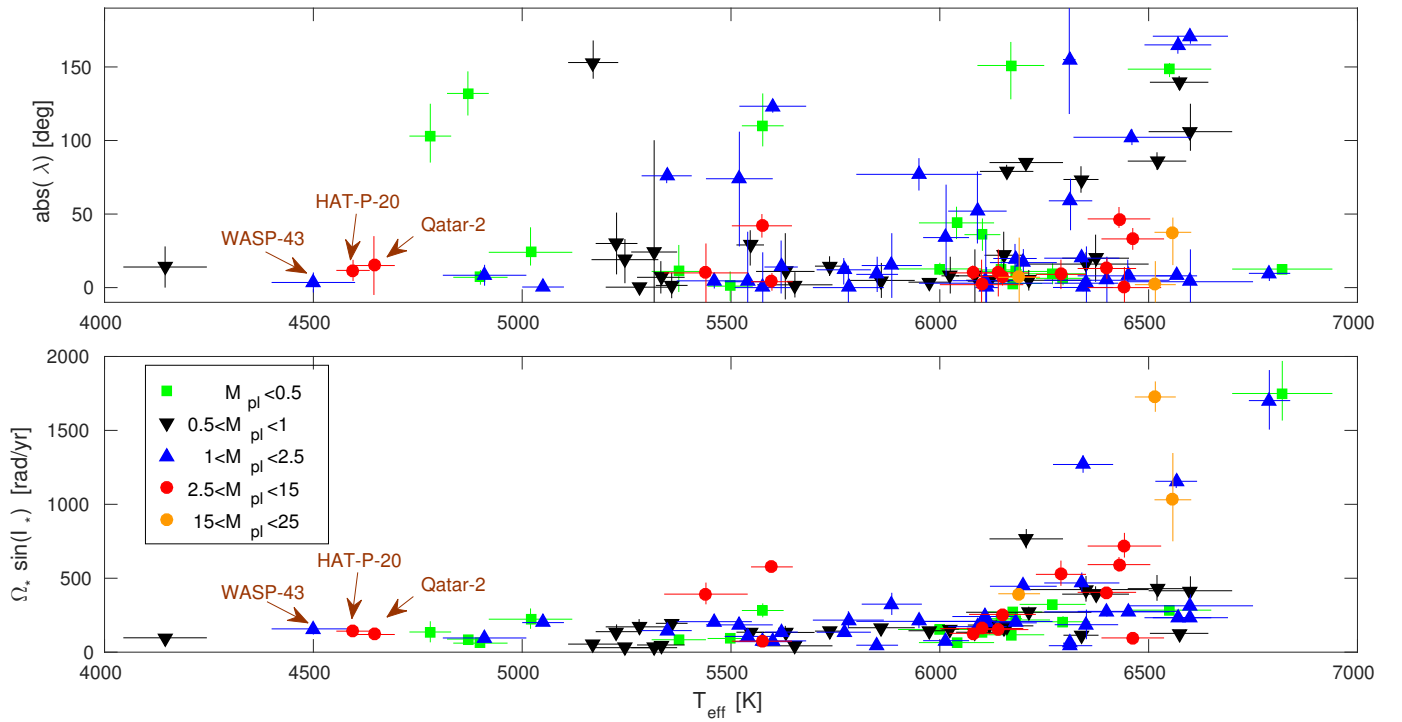


Fig. 8. Top panel: λ - T_{eff} diagram for all the transiting planets with published determinations of λ . Only two systems with $T_{\text{eff}} > 7000$ K were not included. Bottom panel: Projected stellar angular rotational velocity $\Omega_* \sin(i_*)$ as a function of the stellar T_{eff} . We referred to the <http://www.astro.keele.ac.uk/jkt/tepcat/> website for the values of λ , T_{eff} , R_* and M_{pl} ; the values of $V \sin I_*$ were compiled by exploring the literature.

- Baranne, A., Queloz, D., Mayor, M., et al. 1996, *A&AS*, 119, 373
 Barnes, J. W., Linscott, E., & Shporer, A. 2011, *ApJS*, 197, 10
 Baruteau, C., Crida, A., Paardekooper, S.-J., et al. 2014, *Protostars and Planets VI*, 667
 Bate, M. R., Lodato, G., & Pringle, J. E. 2010, *MNRAS*, 401, 1505
 Batygin, K. 2012, *Nature*, 491, 418
 Biazzo, K., D'Orazi, V., Desidera, S., et al. 2012, *MNRAS*, 427, 2905
 Bleic, J., Harrington, J., Madhusudhan, N., et al. 2014, *ApJ*, 781, 116
 Borsa, F., Scandariato, G., Rainer, M., et al. 2015, *A&A*, 578, A64
 Borucki, W. J. 2016, *Reports on Progress in Physics*, 79, 036901
 Boué, G., Montalto, M., Boisse, I., Oshagh, M., & Santos, N. C. 2013, *A&A*, 550, A53
 Bryan, M. L., Alsbai, K. A., Latham, D. W., et al. 2012, *ApJ*, 750, 84
 Canto Martins, B. L., Das Chagas, M. L., Alves, S., et al. 2011, *A&A*, 530, A73
 Chaplin, W. J., Sanchis-Ojeda, R., Campante, T. L., et al. 2013, *ApJ*, 766, 101
 Chen, G., van Boekel, R., Wang, H., et al. 2014, *A&A*, 563, A40
 Claret, A. & Bloemen, S. 2011, *A&A*, 529, A75
 Cosentino, R., Lovis, C., Pepe, F., et al. 2014, in *Society of Photo-Optical Instrumentation Engineers (SPIE) Conference Series*, Vol. 9147, Society of Photo-Optical Instrumentation Engineers (SPIE) Conference Series, 8
 Cosentino, R., Lovis, C., Pepe, F., et al. 2012, in *Society of Photo-Optical Instrumentation Engineers (SPIE) Conference Series*, Vol. 8446, Society of Photo-Optical Instrumentation Engineers (SPIE) Conference Series, 1
 Coughlin, J. L., Mullally, F., Thompson, S. E., et al. 2016, *ApJS*, 224, 12
 Covino, E., Esposito, M., Barbieri, M., et al. 2013, *A&A*, 554, A28
 Cuntz, M., Saar, S. H., & Musielak, Z. E. 2000, *ApJ*, 533, L151
 Cutri, R. M., Skrutskie, M. F., van Dyk, S., et al. 2003, *VizieR Online Data Catalog*, 2246
 Dai, F., Winn, J. N., Yu, L., & Albrecht, S. 2016, *ArXiv e-prints* [arXiv:1609.01314]
 Damasso, M., Biazzo, K., Bonomo, A. S., et al. 2015a, *A&A*, 575, A111
 Damasso, M., Esposito, M., Nascimbeni, V., et al. 2015b, *A&A*, 581, L6
 Damiani, C. & Lanza, A. F. 2015, *A&A*, 574, A39
 Dawson, R. I. 2014, *ApJ*, 790, L31
 Dawson, R. I. & Murray-Clay, R. A. 2013, *ApJ*, 767, L24
 Demarque, P., Woo, J.-H., Kim, Y.-C., & Yi, S. K. 2004, *ApJS*, 155, 667
 Deming, D., Knutson, H., Kammer, J., et al. 2015, *ApJ*, 805, 132
 Desidera, S., Sozzetti, A., Bonomo, A. S., et al. 2013, *A&A*, 554, A29
 D'Orazi, V., Biazzo, K., & Randich, S. 2011, *A&A*, 526, A103
 Eastman, J., Siverd, R., & Gaudi, B. S. 2010, *PASP*, 122, 935
 Esposito, M., Covino, E., Mancini, L., et al. 2014, *A&A*, 564, L13
 Fabrycky, D. C., Lissauer, J. J., Ragozzine, D., et al. 2014, *ApJ*, 790, 146
 Flower, P. J. 1996, *ApJ*, 469, 355
 Gillon, M., Triaud, A. H. M. J., Fortney, J. J., et al. 2012, *A&A*, 542, A4
 Giménez, A. 2006, *ApJ*, 650, 408
 Granata, V., Nascimbeni, V., Piotto, G., et al. 2014, *Astronomische Nachrichten*, 335, 797
 Hartkopf, W. I., Mason, B. D., Finch, C. T., et al. 2013, *AJ*, 146, 76
 Hellier, C., Anderson, D. R., Collier Cameron, A., et al. 2011, *A&A*, 535, L7
 Henden, A. A., Templeton, M., Terrell, D., et al. 2016, *VizieR Online Data Catalog*, 2336
 Hirano, T., Suto, Y., Taruya, A., et al. 2010, *ApJ*, 709, 458
 Hoyer, S., Pallé, E., Dragomir, D., & Murgas, F. 2016, *AJ*, 151, 137
 Hut, P. 1980, *A&A*, 92, 167
 Jackson, B., Barnes, R., & Greenberg, R. 2009, *ApJ*, 698, 1357
 Jiang, I.-G., Lai, C.-Y., Savushkin, A., et al. 2016, *AJ*, 151, 17
 Knutson, H. A., Fulton, B. J., Montet, B. T., et al. 2014, *ApJ*, 785, 126
 Krejčová, T. & Budaj, J. 2012, *A&A*, 540, A82
 Lai, D. 2012, *MNRAS*, 423, 486
 Lanza, A. F. 2008, *A&A*, 487, 1163
 Lanza, A. F. 2012, *A&A*, 544, A23
 Leconte, J., Chabrier, G., Baraffe, I., & Levrard, B. 2010, *A&A*, 516, A64
 Lin, D. N. C., Bodenheimer, P., & Richardson, D. C. 1996, *Nature*, 380, 606
 Lissauer, J. J., Ragozzine, D., Fabrycky, D. C., et al. 2011, *ApJS*, 197, 8
 Lovis, C., Dumusque, X., Santos, N. C., et al. 2011, *ArXiv e-prints* [arXiv:1107.5325]
 Lovis, C. & Pepe, F. 2007, *A&A*, 468, 1115
 Maggio, A., Pillitteri, I., Scandariato, G., et al. 2015, *ApJ*, 811, L2
 Malavolta, L., Nascimbeni, V., Piotto, G., et al. 2016, *A&A*, 588, A118
 Mamajek, E. E. & Hillenbrand, L. A. 2008, *ApJ*, 687, 1264
 Mancini, L., Esposito, M., Covino, E., et al. 2015, *A&A*, 579, A136
 Mancini, L., Southworth, J., Ciceri, S., et al. 2014, *MNRAS*, 443, 2391
 Mazeh, T., Perets, H. B., McQuillan, A., & Goldstein, E. S. 2015, *ApJ*, 801, 3
 McLaughlin, D. B. 1924, *ApJ*, 60
 Metzger, B. D., Giannios, D., & Spiegel, D. S. 2012, *MNRAS*, 425, 2778
 Morton, T. D. & Winn, J. N. 2014, *ApJ*, 796, 47
 Močnik, T., Southworth, J., & Hellier, C. 2016, *ArXiv e-prints* [arXiv:1608.07524]
 Nascimbeni, V., Cunial, A., Murabito, S., et al. 2013, *A&A*, 549, A30
 Nascimbeni, V., Piotto, G., Bedin, L. R., & Damasso, M. 2011, *A&A*, 527, A85
 Nicholson, M. P. 2015, *VizieR Online Data Catalog*, 1330

- Noyes, R. W., Hartmann, L. W., Baliunas, S. L., Duncan, D. K., & Vaughan, A. H. 1984, *ApJ*, 279, 763
- Ogilvie, G. I. 2014, *ARA&A*, 52, 171
- Ogilvie, G. I. & Lin, D. N. C. 2007, *ApJ*, 661, 1180
- Ohta, Y., Taruya, A., & Suto, Y. 2005, *ApJ*, 622, 1118
- Penev, K. M., Hartman, J. D., Bakos, G. A., et al. 2016, *ArXiv e-prints* [arXiv:1606.00848]
- Pepe, F., Mayor, M., Galland, F., et al. 2002, *A&A*, 388, 632
- Poppenhaeger, K., Robrade, J., & Schmitt, J. H. M. M. 2010, *A&A*, 515, A98
- Poretti, E., Boccato, C., Claudi, R., et al. 2016, *Mem. Soc. Astron. Italiana*, 87, 141
- Queloz, D., Eggenberger, A., Mayor, M., et al. 2000, *A&A*, 359, L13
- Ricci, D., Ramón-Fox, F. G., Ayala-Loera, C., et al. 2015, *PASP*, 127, 143
- Rogers, T. M., Lin, D. N. C., & Lau, H. H. B. 2012, *ApJ*, 758, L6
- Rossiter, R. A. 1924, *ApJ*, 60
- Salz, M., Schneider, P. C., Czesla, S., & Schmitt, J. H. M. M. 2015, *A&A*, 576, A42
- Sanchis-Ojeda, R. & Winn, J. N. 2011, *ApJ*, 743, 61
- Schlaufman, K. C. 2010, *ApJ*, 719, 602
- Shkolnik, E. L. 2013, *ApJ*, 766, 9
- Smareglia, R., Bignamini, A., Knapic, C., Molinaro, M., & GAPS Collaboration. 2014, in *Astronomical Society of the Pacific Conference Series*, Vol. 485, *Astronomical Data Analysis Software and Systems XXIII*, ed. N. Manset & P. Forshay, 435
- Snedden, C. 1973, *ApJ*, 184, 839
- Southworth, J. 2011, *MNRAS*, 417, 2166
- Southworth, J., Hinse, T. C., Burgdorf, M., et al. 2014, *MNRAS*, 444, 776
- Southworth, J., Hinse, T. C., Jørgensen, U. G., et al. 2009, *MNRAS*, 396, 1023
- Sozzetti, A., Torres, G., Charbonneau, D., et al. 2007, *ApJ*, 664, 1190
- Suárez Mascareño, A., Rebolo, R., González Hernández, J. I., & Esposito, M. 2015, *MNRAS*, 452, 2745
- Thies, I., Kroupa, P., Goodwin, S. P., Stamatellos, D., & Whitworth, A. P. 2011, *MNRAS*, 417, 1817
- Triaud, A. H. M. J., Gillon, M., Ehrenreich, D., et al. 2015, *MNRAS*, 450, 2279
- Valenti, J. A. & Fischer, D. A. 2005, *ApJS*, 159, 141
- Winn, J. N., Fabrycky, D., Albrecht, S., & Johnson, J. A. 2010a, *ApJ*, 718, L145
- Winn, J. N., Holman, M. J., Henry, G. W., et al. 2007, *AJ*, 133, 1828
- Winn, J. N., Johnson, J. A., Howard, A. W., et al. 2010b, *ApJ*, 723, L223
- Wöllert, M. & Brandner, W. 2015, *A&A*, 579, A129
- Wu, Y. & Lithwick, Y. 2011, *ApJ*, 735, 109
- Wycoff, G. L., Mason, B. D., & Urban, S. E. 2006, *AJ*, 132, 50
- Zacharias, N., Finch, C., Subasavage, J., et al. 2015, *AJ*, 150, 101
- Zuckerman, B. & Song, I. 2004, *ARA&A*, 42, 685

Appendix A: RV tables

Table A.1. HARPS-N RV data for WASP-43. The columns report: BJD (TDB), the mid-exposure Barycentric Julian Dates in Barycentric Dynamical Time; T_{exp} , the exposure time; RV and error are the radial velocity measurement and its estimated uncertainty; FWHM, the Full Width at Half Maximum of the Cross-Correlation Function; Bis. Span, the radial velocity bisector span of the CCF; Airmass, the airmass of the star at the beginning of the exposure; Flag, indicating whether the spectrum was taken in-transit (i) or off-transit (o).

BJD (TDB)	T_{exp} [sec]	RV [km s ⁻¹]	error [km s ⁻¹]	FWHM [km s ⁻¹]	Bis. Span [km s ⁻¹]	Airmass	Flag
2456363.415882	450	-3.2736	0.0111	7.17	0.086	1.59	o
2456363.421396	450	-3.3145	0.0120	7.15	0.076	1.55	o
2456363.426923	450	-3.3185	0.0115	7.16	0.027	1.51	o
2456363.432437	450	-3.3278	0.0096	7.18	0.015	1.48	o
2456363.437951	450	-3.3683	0.0093	7.14	0.060	1.45	o
2456363.443460	450	-3.3820	0.0091	7.16	0.056	1.42	o
2456363.448974	450	-3.4072	0.0092	7.25	0.046	1.40	o
2456363.454484	450	-3.4373	0.0093	7.16	0.056	1.38	o
2456363.459988	450	-3.4560	0.0088	7.17	0.057	1.36	o
2456363.465502	450	-3.4526	0.0095	7.16	0.102	1.34	i
2456363.471016	450	-3.5011	0.0099	7.12	0.034	1.33	i
2456363.476525	450	-3.4876	0.0096	7.16	0.079	1.31	i
2456363.482039	450	-3.5192	0.0096	7.20	0.057	1.30	i
2456363.487549	450	-3.5517	0.0094	7.19	0.057	1.29	i
2456363.493054	450	-3.5978	0.0093	7.17	0.080	1.29	i
2456363.498567	450	-3.6221	0.0102	7.14	0.024	1.28	i
2456363.504081	450	-3.6596	0.0091	7.15	0.071	1.28	i
2456363.509590	450	-3.6773	0.0086	7.14	0.023	1.28	i
2456363.515104	450	-3.6747	0.0090	7.19	0.060	1.28	i
2456363.520614	450	-3.6976	0.0097	7.23	0.005	1.28	o
2456363.526123	450	-3.7218	0.0103	7.18	0.032	1.28	o
2456363.531624	450	-3.7571	0.0109	7.22	0.025	1.29	o
2456363.537128	450	-3.7764	0.0113	7.17	0.043	1.30	o
2456363.542642	450	-3.7869	0.0104	7.13	0.062	1.30	o
2456363.548156	450	-3.8216	0.0113	7.21	0.050	1.31	o
2456363.553670	450	-3.8339	0.0132	7.18	0.076	1.33	o
2456363.559179	450	-3.8659	0.0117	7.16	0.073	1.34	o
2456363.564693	450	-3.8770	0.0154	7.22	0.106	1.36	o
2456363.571207	450	-3.8913	0.0144	7.26	0.083	1.38	o
2456363.576712	450	-3.9012	0.0121	7.18	0.068	1.40	o
2456363.582230	450	-3.9561	0.0163	7.17	0.082	1.43	o
2456363.587740	450	-3.9589	0.0127	7.15	0.048	1.46	o
2456376.517002	900	-3.6434	0.0058	7.27	0.034	1.33	i
2456377.589657	900	-4.1247	0.0088	7.40	-0.093	1.81	o
2456381.558437	450	-4.0933	0.0088	7.19	0.072	1.59	o
2456381.563762	450	-4.1130	0.0089	7.18	0.030	1.64	o
2456382.512779	900	-3.9513	0.0052	7.20	0.041	1.37	o
2457050.557137	900	-3.2261	0.0192	7.18	0.101	1.43	o
2457116.447829	900	-3.2458	0.0045	7.11	0.075	1.28	o
2457145.424807	900	-4.1267	0.0154	7.02	0.052	1.38	o

Table A.2. HARPS-N RV data for HAT-P-20. See the caption of Table A.1 for the meaning of the columns.

BJD (TDB)	T _{exp} [sec]	RV [km s ⁻¹]	error [km s ⁻¹]	FWHM [km s ⁻¹]	Bis. Span [km s ⁻¹]	Airmass	<i>z</i>
2456252.743420	900	-17.8116	0.0034	7.02	0.073	1.05	o
2456305.646766	900	-17.6177	0.0030	7.01	0.039	1.17	o
2456323.675026	900	-19.2777	0.0082	7.12	0.046	1.79	o
2456569.727872	900	-16.8530	0.0031	7.03	0.055	1.15	o
2456581.752206	900	-17.8062	0.0026	7.05	0.050	1.02	o
2456606.758475	1200	-16.9772	0.0039	7.08	0.026	1.03	o
2456608.768700	900	-19.0709	0.0025	7.10	0.064	1.05	o
2456608.778237	400	-19.0600	0.0045	7.10	0.057	1.06	o
2456609.779656	900	-16.8533	0.0056	7.06	0.050	1.08	o
2456621.746725	1200	-17.1818	0.0030	7.12	0.036	1.08	o
2456622.723432	900	-19.3090	0.0035	7.12	0.056	1.03	o
2456631.627655	900	-19.2637	0.0024	7.01	0.068	1.01	o
2456719.481675	900	-17.1670	0.0063	7.11	0.054	1.08	o
2456723.544801	900	-19.2887	0.0036	7.10	0.048	1.43	o
2456728.410880	600	-17.8740	0.0046	7.05	0.009	1.01	o
2456728.418111	600	-17.8955	0.0046	7.08	0.027	1.01	o
2456728.425345	600	-17.9150	0.0046	7.07	0.017	1.02	o
2456728.432580	600	-17.9264	0.0046	7.09	0.013	1.03	o
2456728.439814	600	-17.9500	0.0050	7.09	-0.014	1.04	o
2456728.447035	600	-17.9705	0.0050	7.08	-0.001	1.06	i
2456728.454265	600	-17.9766	0.0046	7.09	0.016	1.07	i
2456728.461495	600	-17.9831	0.0044	7.06	0.005	1.09	i
2456728.468729	600	-18.0035	0.0041	7.07	0.033	1.11	i
2456728.475959	600	-18.0383	0.0046	7.07	0.023	1.13	i
2456728.483184	600	-18.0725	0.0048	7.08	0.030	1.16	i
2456728.490418	600	-18.0874	0.0057	7.07	0.030	1.18	i
2456728.497653	600	-18.1251	0.0062	7.12	0.011	1.22	i
2456728.504882	600	-18.1492	0.0052	7.07	0.027	1.25	i
2456728.512125	600	-18.1571	0.0052	7.06	0.015	1.29	i
2456728.519346	600	-18.1668	0.0054	7.08	0.010	1.33	i
2456728.526585	600	-18.1851	0.0056	7.05	0.009	1.38	o
2456728.533816	600	-18.2109	0.0054	7.06	0.033	1.44	o
2456728.541041	600	-18.2263	0.0065	7.16	-0.006	1.50	o
2456728.548267	600	-18.2480	0.0076	7.15	0.016	1.57	o
2456728.555489	600	-18.2684	0.0071	7.17	-0.008	1.65	o
2456728.562718	600	-18.2802	0.0079	7.20	0.005	1.75	o
2456728.569953	600	-18.3064	0.0091	7.16	-0.018	1.85	o
2456976.687433	900	-19.2139	0.0022	6.95	0.043	1.01	o
2457005.717112	900	-18.7385	0.0043	6.94	0.072	1.13	o
2457011.702769	900	-18.1656	0.0036	6.96	0.065	1.14	o
2457125.412095	900	-18.4303	0.0020	7.04	0.068	1.25	o
2457389.617073	900	-17.5685	0.0045	7.05	0.063	1.02	o

Notes. ^(†) i ≡ in-transit, o ≡ out-of-transit

Table A.3. HARPS-N RV data for Qatar-2. See the caption of Table A.1 for the meaning of the columns.

BJD (TDB)	T _{exp} [sec]	RV [km s ⁻¹]	error [km s ⁻¹]	FWHM [km s ⁻¹]	Bis. Span [km s ⁻¹]	Airmass	\tilde{r}
2456775.434193	900	-23.7480	0.0271	6.69	0.089	1.51	o
2456775.444895	900	-23.7285	0.0265	6.65	0.025	1.44	o
2456775.455598	900	-23.8385	0.0307	6.69	0.081	1.38	o
2456775.466305	900	-23.8248	0.0261	6.72	-0.004	1.34	o
2456775.477012	900	-23.8530	0.0253	6.75	0.089	1.30	o
2456775.487705	900	-23.8691	0.0305	6.73	-0.069	1.27	i
2456775.498412	900	-23.8725	0.0271	6.72	0.132	1.25	i
2456775.509114	900	-23.9181	0.0242	6.73	-0.011	1.24	i
2456775.519825	900	-23.9703	0.0254	6.60	0.038	1.23	i
2456775.530532	900	-24.0137	0.0225	6.74	-0.008	1.23	i
2456775.541239	900	-24.0664	0.0304	6.74	0.012	1.23	i
2456775.551946	900	-24.0915	0.0374	6.59	0.111	1.24	i
2456775.562648	900	-24.0793	0.0407	6.67	0.055	1.26	i
2456775.573355	900	-24.1343	0.0432	6.71	0.015	1.28	o
2456775.584062	900	-24.1286	0.0409	6.80	0.000	1.32	o
2456775.594760	900	-24.1363	0.0361	6.72	-0.030	1.35	o
2456775.605458	900	-24.2294	0.0386	6.69	0.052	1.40	o

Notes. ^(†) i \equiv in-transit, o \equiv out-of-transit